RSC Advances

PAPER

Cite this: *RSC Adv.*, 2024, **14**, 12158

Reduced graphene oxide/MXene hybrid decorated graphite felt as an effective electrode for vanadium redox flow battery†

Zhihui Li, Wei Yang,* Jingjing Bao,* Youmei Kong, Shangchen Jing, Jingying Zhang, Guanhua Ren, Licheng Sun and Min Du

Vanadium redox flow battery (VRFB) is a highly suitable technology for energy storage and conversion in the application of decoupling energy and power generation. However, the sluggish reaction kinetics of redox couples is one of the bottlenecks hindering the commercialization of VFFBs. Developing efficient electrode is a promising method to improve the battery performance. In this work, a reduced graphene oxide/Mxene hybrid-decorated graphite felt (rGO/Mxene@GF) is designed to facilitate the kinetics of redox reaction. The electrocatalytic activity and mass transfer of the prepared electrode are investigated through experiment and simulation methods. The results indicate that the favorable mass transfer and the synergistic effect between rGO and $Ti_3C_2T_x$ Mxene remarkably improve the performance of electrode. The flow cell with rGO/Mxene@GF delivers a good stability up to 100 cycles with a coulombic, voltage, and energy efficiency of 91.6%, 82.7%, and 75.8%, respectively, at a current density of 80 mA cm^{-2}. These findings suggest that the as-prepared rGO/Mxene@GF holds a good application potential in VRFB and provides a promising approach to design efficient electrode for electrochemical devices.

Received 20th February 2024
Accepted 25th March 2024

DOI: 10.1039/d4ra01306a

rsc.li/rsc-advances

1. Introduction

Global climate change and energy crisis have severely threatened the sustainability of human society. The development of renewable energy power (such as wind and solar power) is an effective approach to addressing above issues.[1–3] However, the intrinsic intermittence and fluctuation of renewable energy power affect the stability of grid when directly integrating into the grid. Therefore, it is essential to develop energy storage systems to store the intermittent and fluctuating electricity for subsequent utilizations.[4–6] Among various technologies, the vanadium redox flow battery (VRFB) exhibits the features of stable cycling performance, high battery capacity, flexible design, and overall structural safety, emerging as one of the most promising energy storage devices for grid energy storage and distribution.[7,8]

Despite significant progress in the development of VRFB over the past few decades, the widespread commercialization of this technology still faces economic and technical challenges, including the expensive components of the battery and low performance.[9,10] As the core components of VRFB, the electrodes play a crucial role in facilitating the redox reaction kinetics and improving the performance of battery.[11] Although the traditional planar electrode such as graphite flake has been widely used for VRFB, but their low surface area limited the electrochemical reaction and electron transfer pathways, resulting in a lower overall performance of energy storage. Importantly, the three-dimensional porous electrodes can offer advantages such as a high porosity and a reasonable pore size distribution, providing more mass transfer channels and larger surface area for electrochemical reactions during energy storage.[12–14] Among various three-dimensional electrodes, graphite felt electrodes are commonly used in VRFB due to their wide working potential range, good stability, high conductivity, high corrosion resistance, and relatively low cost. However, the utilization of graphite felt still faces challenges due to its poor electrochemical activity, leading to insufficient active sites for vanadium redox reactions.[15,16]

To improve the reaction kinetics of three-dimensional porous electrodes, various methods have been reported, including surface modifications to introduce chemical groups (*e.g.*, thermal treatment,[17] acid treatment,[18] and microwave radiation treatment[19]), surface etching to improve the surface area or pore structures (CO_2 etching,[20,21] water etching,[22] KOH etching[23,24]), and catalyst loading to enhance catalytic activity of electrode. Among these methods, loading catalysts on electrode to enhance electrode reaction kinetics is the most effective and commonly used approach. In the past decades, many carbon-

State Key Laboratory of Hydraulics and Mountain River Engineering, College of Water Resource & Hydropower, Sichuan University, Chengdu 610065, China. E-mail: wei_yang@scu.edu.cn; baojj247@scu.edu.cn

† Electronic supplementary information (ESI) available. See DOI: https://doi.org/10.1039/d4ra01306a

based catalysts such as carbon nanoparticles, carbon nanotubes, carbon flakes, carbon spheres, and metal-based nanoscale catalysts such as Bi, Sn, Cu, TiC, TiN, TiO_2, CeO_2, ZrO_2, Mn_3O_4 *etc.* have been reported to improve battery performance.[25–27] For example, González *et al.*[28] prepared a graphene-graphite composite electrode using an electrophoretic deposition method. The modified graphite felt exhibited an improved electrochemical activity and kinetic reversibility for the VO^{2+}/VO_2^+ redox couple with a high energy efficiency of 95.80% at a current density of 25 mA cm^{-2}. Wu *et al.*[29] used pulse electrodeposition to incorporate PbO_2 onto the surface of graphite felt. The modified graphite felt electrode exhibited an enhanced activity for vanadium ion electrochemical reactions. The assembled battery using this electrode achieved an energy efficiency of 82.4% at a current density of 70 mA cm^{-2}.

Among the various catalysts, $Ti_3C_2T_x$ MXene is a highly conductive and hydrophilic electrode material with various types of surface terminations such as fluorine, oxygen, and hydroxyl groups. Due to its unique structure, surface chemical properties, outstanding mechanical stability and metal conductivity, $Ti_3C_2T_x$ is regarded as a promising catalyst for VFRBs.[30] Wei *et al.*[31] were the first to use $Ti_3C_2T_x$ as an electrocatalyst to promote the V^{2+}/V^{3+} redox reactions, they created a $Ti_3C_2T_x$ hollow sphere structure to mitigate the stacking of MXene layers, the results showed that the battery with the prepared electrode achieved an electrolyte utilization efficiency and energy efficiency of 80.1% and 81.3%, which were 41.7% and 15.7% higher than that of pristine electrode. However, the layered $Ti_3C_2T_x$ materials suffer from the reduced surface area due to the re-stacking of 2D nanosheets during the electrode preparation. This significantly decreases the specific surface area and limits the mass transport of electrolyte ions, consequently declining the performance of the electrode.[32,33] In addition, above method involves multiple processing steps and is relatively complex, and the incorporation of $Ti_3C_2T_x$ onto substrate generally uses the nonconductive and hydrophobic ionomers (*e.g.*, Nafion) as binders, resulting a lowered electron transfer efficiency and electrolyte transport. Notably, graphene is a 2D nanomaterials with a large surface area, an excellent electric conductivity and exceptional ion storage capability, constructing the composite or hybrid of $Ti_3C_2T_x$ with graphene can be an effective method to address the issues of limited ion transport and surface area resulting from the re-stacking of MXene.[34–36] The binder-free electrode based on carbon felt can mitigate the insufficient electron transfer and electrolyte transport due to the utilization of hydrophobic ionomers.

Based on above consideration, we herein proposed rGO/Mxene hybrid for the construction of graphitic felt electrode. During the preparation, irregular $Ti_3C_2T_x$ MXene particles can be first embedded and dispersed within the graphene layers, thus alleviating the re-stacking of $Ti_3C_2T_x$ and increasing the exposure of active sites. An improved electrochemical activity and mass transport of ions can be realized by *in situ* incorporating rGO/Mxene hybrid onto the skeleton of graphite felt without the use of binders. The physicochemical properties and electrochemical performance of the prepared electrode were comprehensively characterized. The results indicated that the synergistic effect between rGO and MXene, and favorable mass transfer significantly enhanced the performance of electrode. The VFRB with rGO/Mxene@GF electrode exhibited a good stability of 100 cycles with a coulombic, voltage, and energy efficiency of 91.6%, 82.7%, and 75.8% at a current density of 80 mA cm^{-2}. These results suggested a good application potential of the as-prepared rGO/Mxene@GF in VRFB.

2. Experimental section

2.1 Synthesis of $Ti_3C_2T_x$ suspension

A solution containing $Ti_3C_2T_x$ MXene flakes was obtained by selectively etching Ti_3AlC_2 precursors according to the wet chemical methods reported by Gogotsi.[37] In detail, 2 g of LiF was added into 40 mL of 9 M HCl to prepare a well-mixed solution. Subsequently, 2 g of Ti_3AlC_2 powder was slowly added into above solution under ice bath condition. After stirring at 35 °C for 24 h, the mixed solution was collected and followed by repeated washing with deionized water and centrifugation until the pH 6. The resulting multilayer $Ti_3C_2T_x$ was re-mixed with deionized water and ultrasonicated for 1 h in a nitrogen atmosphere. After centrifugation at 3500 rpm for 40 min, the supernatant containing $Ti_3C_2T_x$ dispersion was collected. To determine the concentration of the $Ti_3C_2T_x$ dispersion, 10 mL of solution was filtered through vacuum filtration to obtain the Mxene sample, which was then vacuum-dried at 70 °C. The obtained Mxene was peeled off from the filtration membrane and weighed to determine the concentration of the $Ti_3C_2T_x$ solution.

2.2 Synthesis of GO/MXene hybrid

Graphene oxide was synthesized according to the modified Hummers' method.[38] The prepared GO was dissolved into deionized water and sonicated to obtain a 1 mg mL^{-1} GO solution. After that, 1 mg mL^{-1} of $Ti_3C_2T_x$ dispersion was prepared using the similar method, and GO and $Ti_3C_2T_x$ solution was mixed (1 : 1 v : v) to create a mixture of GO and $Ti_3C_2T_x$. The mixture was further ultrasonicated to obtain a homogeneous GO/Mxene solution.

2.3 Fabrication of rGO/Mxene-decorated graphite felt electrodes

The purchased graphite felt (GF) was cut into pieces with dimensions of 3 × 2 × 0.4 cm. These graphite felt pieces were immersed into an ethanol/water (1 : 1 v : v) solution, followed by ultrasonic treatment for 30 min. Subsequently, the graphite felt pieces were cleaned using deionized water and dried in a convection oven at 60 °C. For the synthesis of rGO/Mxene@GF, the prepared GF was immersed in 60 mL of homogeneous GO/Mxene solution. The mixture was then transferred into a 100 mL Teflon-lined autoclave and hydrothermally treated at 180 °C for 6 h. After cooling down to room temperature, the samples were vacuum-dried and annealed in a tube furnace at 400 °C for 1 h in nitrogen atmosphere at a heating rate of 5 °C min^{-1}. After cooling to room temperature, the samples were collected and washed using deionized water.

The schematic diagram of the rGO/Mxene@GF fabrication is elucidated in Fig. 1. For comparison, rGO@GF and Mxene@GF were prepared through the same procedure by using rGO and Mxene solution, respectively. The original graphite felt was used as the control sample and named as GF.

2.4 Physical characterization

Morphologies of the fabricated electrodes were characterized using scanning electron microscopy (SEM, Gemini SEM 360, Germany). Furthermore, elemental mapping analysis was conducted using an energy-dispersive (EDS) (OXFORD X-MAS, UK) attached to the SEM scope. X-ray diffraction (XRD) patterns were acquired with a Ultima IV powder X-ray diffractometer (Rigaku Corporation, Japan) equipped with Cu-Kα radiation at the scan rate of 5 min^{-1} from $2\theta = 10°$ to 90°. X-ray photoelectron spectroscopy (XPS) measurements were conducted using a Thermo Scientific ESCALAB 250Xi spectrometer with K-Alpha. Fourier-transform infrared (FT-IR) spectra were obtained on an IS5 spectrophotometer (Thermo Fisher Scientific, USA) over the range of 600–4000 cm^{-1}. Raman spectroscopy were collected on a Thermo DXR2xi (Thermo Fisher Scientific, USA) using an Ar ion laser with an excitation wavelength of 532.0 nm.

The as prepared electrode was scanned and imaged using X-ray computed tomography (Phoenix-ge V tome S240/180, England), the three-dimensional morphology of the fibers was reconstructed based on two-dimensional superposition using threshold segmentation technology in AVIZO software. The original scanning volume is 3.5 × 3.5 × 1 mm. To reduce the complexity of calculation, a piece of 0.5 × 0.5 × 0.5 mm was collected for calculation. The volume porosity of 87.5% was obtained for reconstructed model. The fiber phase and pore phase two-phase model were obtained by using the AVIZO software through the interactive thresholding, and the pore phase was used as the liquid phase. The reconstructed electrode pore model was obtained by using Boolean operation to invert the reconstructed electrode microstructure, and then the pixel model was smooth processed and converted into mesh model, which was then imported into COMSOL software to repair mesh defects. The mesh model includes 6 334 152 tetrahedral mesh units, 1 001 002 triangular grid cells and 12 232 side grid cells. The detailed description of model and parameter was shown in ESI.†

2.5 Electrochemical characterization

Electrochemical measurements were conducted using a typical three-electrode setup on an electrochemical workstation (Multi Autolab M204, Netherlands), using platinum foil as the working electrode, saturated calomel electrode (SCE) as the reference electrode, and the prepared graphite felt as the working electrode. Cyclic voltammetry (CV) and electrochemical impedance spectroscopy (EIS) tests were performed in 0.1 M VO^{2+} + 3 M H_2SO_4 solution and 0.1 M V^{3+} + 3 M H_2SO_4 solution, respectively. The CV was scanned from 0.5 to 1.3 V *vs.* SCE and −0.9 to −0.2 V *vs.* SCE for VO^{2+}/VO_2^+ and V^{2+}/V^{3+} redox reaction at a scan rate of 3 mV s^{-1}. EIS tests were carried over a frequency range from 10^5 to 0.1 Hz with a sinusoidal perturbation signal amplitude of 10 mV at fixed potentials of 0.86 V and −0.5 V, respectively.

2.6 Battery performance

Performance of the prepared electrodes was evaluated using a custom-made flow battery with an S-shaped flow field design. Nafion 117 membrane was employed as ion exchange membrane. The schematic diagram of battery design was shown in Fig. 2. In this configuration, the prepared graphite felt electrodes with dimensions of 1.6 × 1.6 cm^2 were used as both the anode and cathode. The anolyte (10 mL 1.7 M VO^{2+} in 4 M

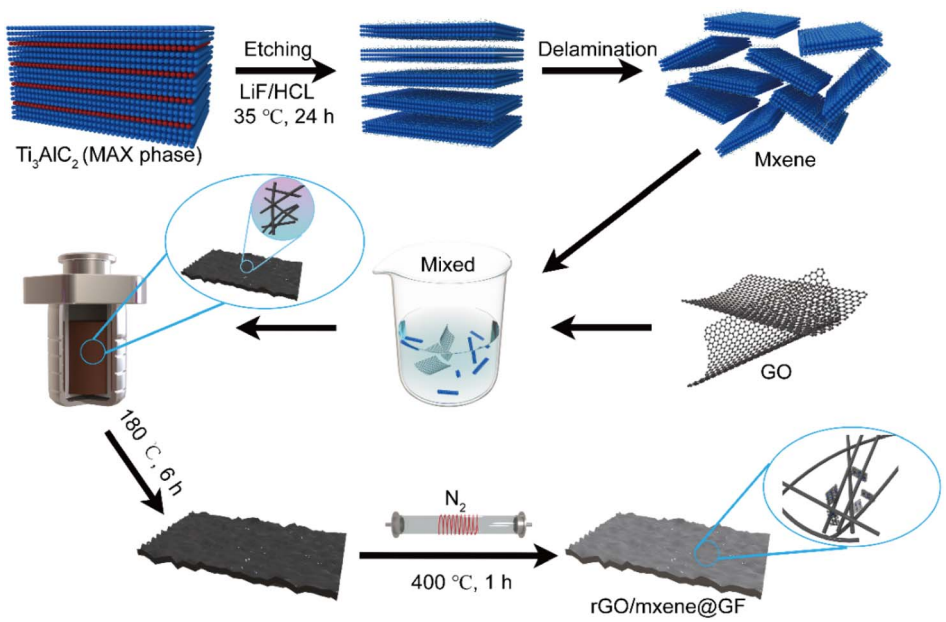

Fig. 1 Schematic diagram of rGO/Mxene@GF synthesis process.

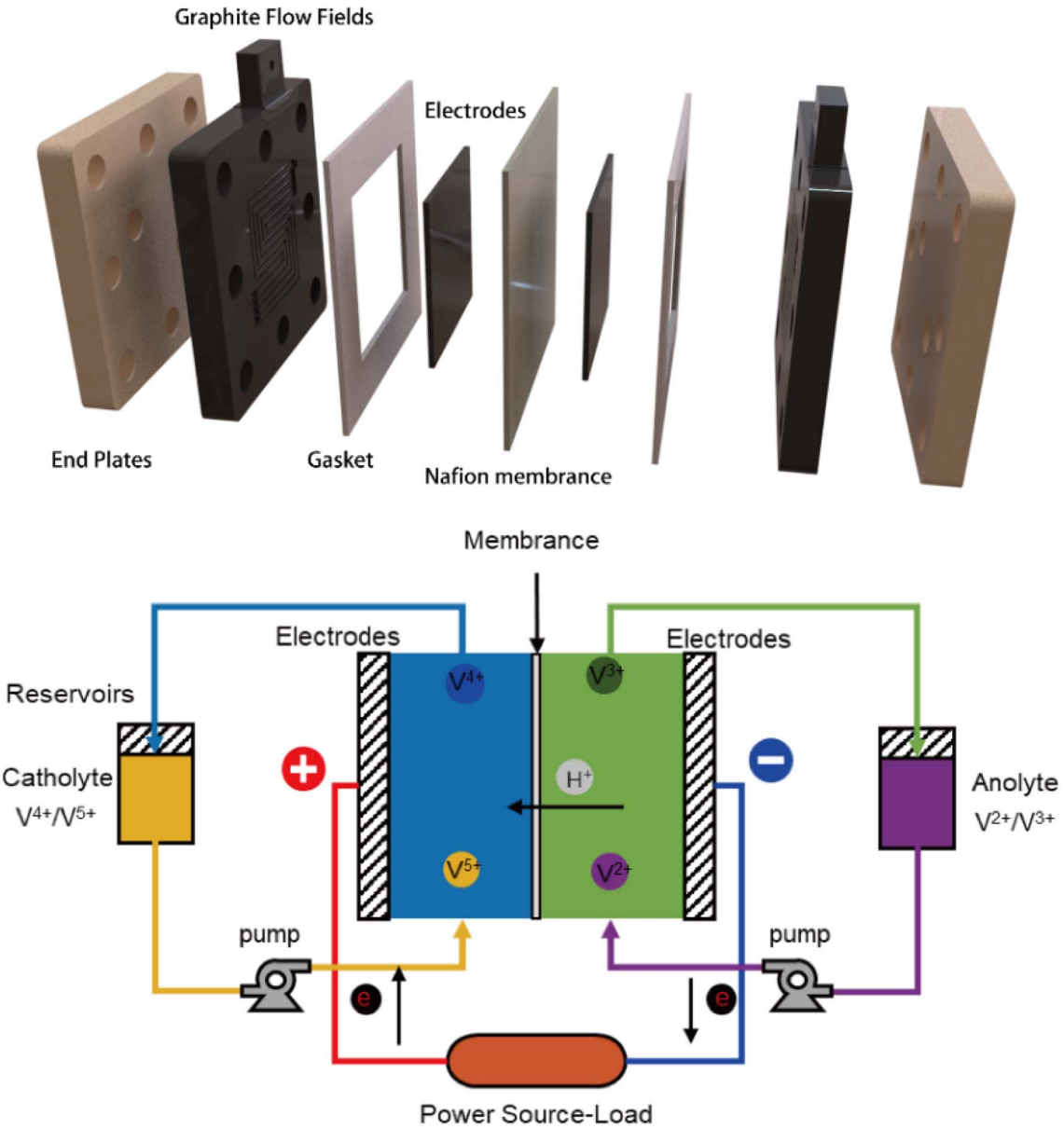

Fig. 2 Picture and scheme of VFRBs.

H_2SO_4) and catholyte (10 mL 1.7 M V^{3+} in 4 M H_2SO_4) were circulated at a constant flow rate of 50 mL min^{-1}. The performance of batteries was tested by charging to a cut-off voltage of 1.65 V and discharging to a cut-off voltage of 0.8 V at current densities of 40, 60 and 80 mA cm^{-2}. All measurements were performed at room temperature.

3. Results and discussion

3.1 Physical characteristics

Morphologies of the prepared electrode were characterized using SEM. As shown in Fig. 3a, the pre-treated original GF exhibits a fine texture composing of smooth carbon fibers, indicating that the pre-treatment process effectively removed impurities from carbon felt surface. Fig. 3b depicts the rGO-doped GF after the hydrothermal reaction, one can see that the surface of carbon fibers is coated with a layer of material at higher magnification of SEM. This suggests that rGO was grown on the GF surface during hydrothermal treatment. Similarly, the Mxene can be also attached onto the carbon fibers of GF after hydrothermal reaction (Fig. 3c). Notably, the Mxene exhibited a layered structure after the etching, similar to the literature reported (Fig. S1†).[39] On the basis of layered structure of GO and Mxene, the rGO/Mxene hybrid finally formed an interlocking structure of nanosheets (Fig. 3e). The interlocking nanosheet structure of rGO/Mxene hybrid was then closely grown on the surface of carbon fibers in the GF (Fig. 3d). The layered rGO/Mxene hybrid can not only increase the exposure of active sites for redox reactions, but also improve the mass transport of ions, thereby improving the electrochemical performance of the

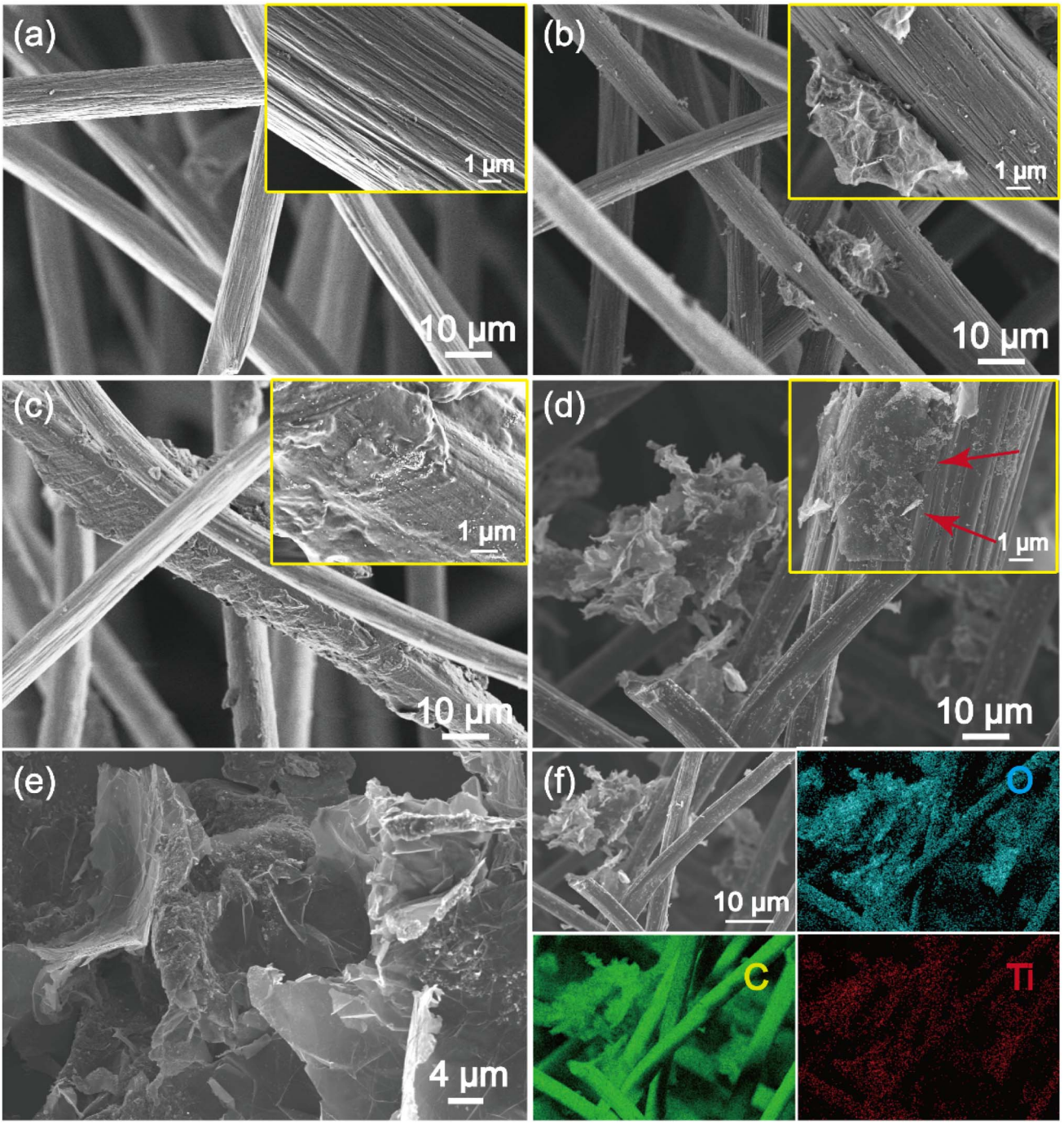

Fig. 3 SEM images of (a) GF, (b) rGO@GF, (c) Mxene@GF, (d) rGO/Mxene@GF, (e) rGO/Mxene, (f) elemental mappings of rGO/Mxene@GF.

electrode. Furthermore, elemental mapping analysis based on EDS exhibits a homogeneous distribution of C, O and Ti in rGO/Mxene@GF (Fig. 3f), indicating the successful incorporation of rGO/Mxene to the graphite felt fibers with a C, O and Ti content of 81.7 wt%, 14.7 wt% and 3.5 wt%, as reflected by EDS spectrum (Fig. S2†). The incorporation of heteroatoms can regulate the microstructure and chemical properties of electrode, consequently changing the electrochemical redox reaction kinetics.

The microstructure of the prepared electrodes was evaluated using XRD. As depicted in Fig. 4a, it can be seen that the electrodes fabricated using different processes exhibited a broad diffraction peak at 26.5° and 44.5°, which can be assigned to the (002) and (100) crystal planes of graphitized carbon separately, consistent with the literatures.[40] It should be noted that the characteristic peaks of Mxene were not clear due to the coverage of intensive graphitized carbon (002) peaks, because the content of graphitized carbon was much higher than Mxene. However, some minor peaks can still be observed at ~37.7° and ~46.3°

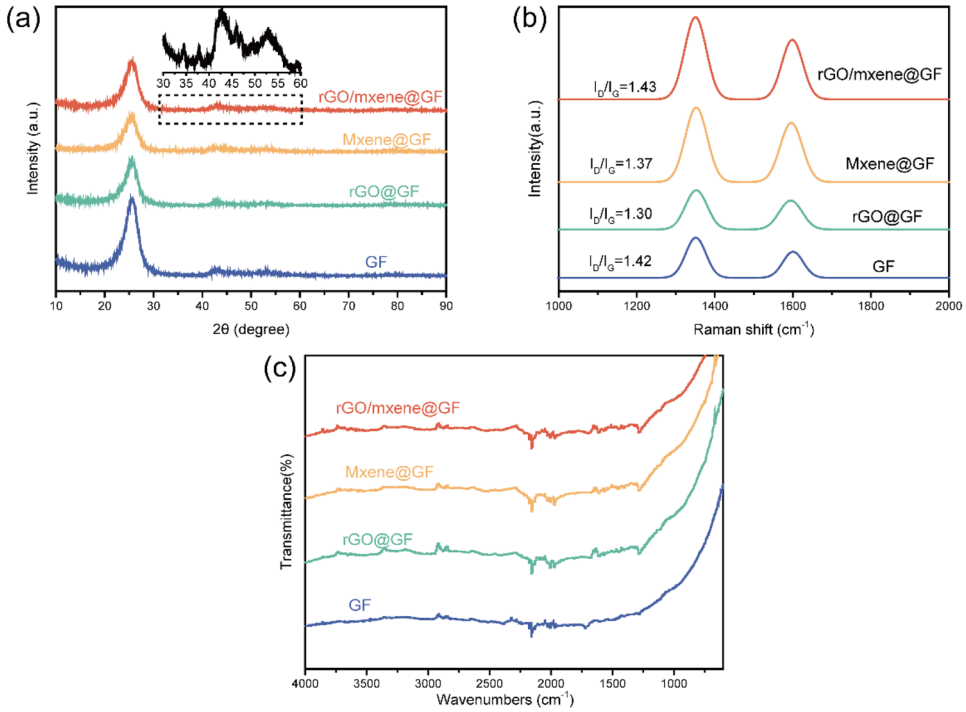

Fig. 4 (a) XRD spectra, (b) Raman spectra and (c) FT-IR spectrum of different electrodes.

(Fig. 4a), which were corresponded to the (103) and (106) phases of $Ti_3C_2T_x$.[41] This confirms that the Mxene was indeed incorporated on to the GF. In addition, the graphitization degree and defects of various electrodes were further evaluated using Raman spectrum. As shown in Fig. 4b, all samples exhibit two typical peaks identified at 1352.7 and 1597.4 cm^{-1}, corresponding to D- and G-band respectively. The D-band is the vibration of sp^3 defect site in C atom, while the G-band is the vibration of sp^2 bonded atom. The graphitization degree of samples can be quantified by the intensity ratio of the D and G bands (I_D/I_G). From the Raman spectrum, the I_D/I_G was calculated to be 1.43 for rGO/Mxene@GF, 1.31 for rGO@GF, 1.37 for Mxene@GF, and 1.42 for GF, separately. This indicates that the introduction of Mxene/rGO composite materials onto the GF increased defects on the electrode surface. Previous studies have reported that the incorporation of heteroatom would increase the defects in the carbon frameworks, and hence provide more possible active site for electrochemical reactions.[40]

Furthermore, FT-IR spectrum was collected to confirm the functional groups on the surface of electrodes, as shown in Fig. 4c. It is clear that the FT-IR spectrum of rGO/Mxene@GF exhibits peaks at 3437 cm^{-1}, 1636 cm^{-1}, 620 cm^{-1}, 1097 cm^{-1}, and 1399 cm^{-1}, corresponding to the absorption of H_2O, –OH, Ti–O, C–F, and O–H, respectively, indicating the presence of Mxene.[42] The FT-IR spectrum of rGO/GF shows absorption peaks at 3385 cm^{-1}, 1730 cm^{-1}, 1625 cm^{-1}, 1409 cm^{-1}, 1170 cm^{-1}, 1042 cm^{-1}, and 876 cm^{-1}, corresponding to –OH, C=O, C=C, C–OH, C–O, C–H, and C–O–C vibrations. These peaks also confirm the presence of rGO.[43] These results suggest the successful incorporation of rGO and $Ti_3C_2T_x$ Mxene on to the surface of electrode. Notably, C–F probed in rGO/Mxene@GF plays a positive role in enhancing the electrochemical performance, render the materials a promising candidates for electrocatalysts in vanadium redox reactions.

To evaluate the elemental composition and their valence states on the surface of electrode, the XPS measurement was conducted. From the XPS full spectra of electrodes, one can see that C 1s (~284.5 eV) and O 1s (~532.0 eV) were observed for all samples, and Ti 2p (~460.0 eV) was identified for Mxene@GF and rGO/Mxene@GF (Fig. 5a). The elemental content of C, O and Ti was calculated to be 85.6 at%, 13.2 at% and 1.2 at%, respectively, according to XPS measurement (Fig. S3†). This further indicates that the Mxene had been doped into the GF successfully. The high-resolution spectra of C 1s are depicted in Fig. 5b, the spectra can be divided into 3 different peaks, which were assigned to sp^2 hybrid C–C bond at 284.7 eV, C–O bonds at 285.4 eV, and O–C=O bonds at 288.9 eV. As shown in Fig. 5c, the deconvolution of O 1s exhibited two peaks at 532.3 eV and 533.5 eV for all samples, corresponding to C=O bonds and C–O bonds respectively. However, it should be noted that characteristic peaks at 530.2 and 531.7 eV were appeared for Mxene@GF and rGO/Mxene@GF, which can be assigned to Ti–C–O_x and TiO_2, respectively.[44] This can be also verified by the XPS high-resolution spectrum of Ti 2p. From Fig. 5d, one can see that the spectrum exhibited three pairs of peaks ascribing to the Ti $2p_{1/2}$ and Ti $2p_{3/2}$. The first doublet at 458.7/464.0 eV was the Ti^{2+}, and the one at 459.1/464.3 eV was the Ti^{3+}, whereas the peaks at 459.6/464.9 eV were due to the presence of TiO_2.[45,46] All of these physicochemical characterizations suggested that the as-prepared rGO/Mxene@GF exhibited a well formed layered structure on the skeleton of carbon fibers, and the

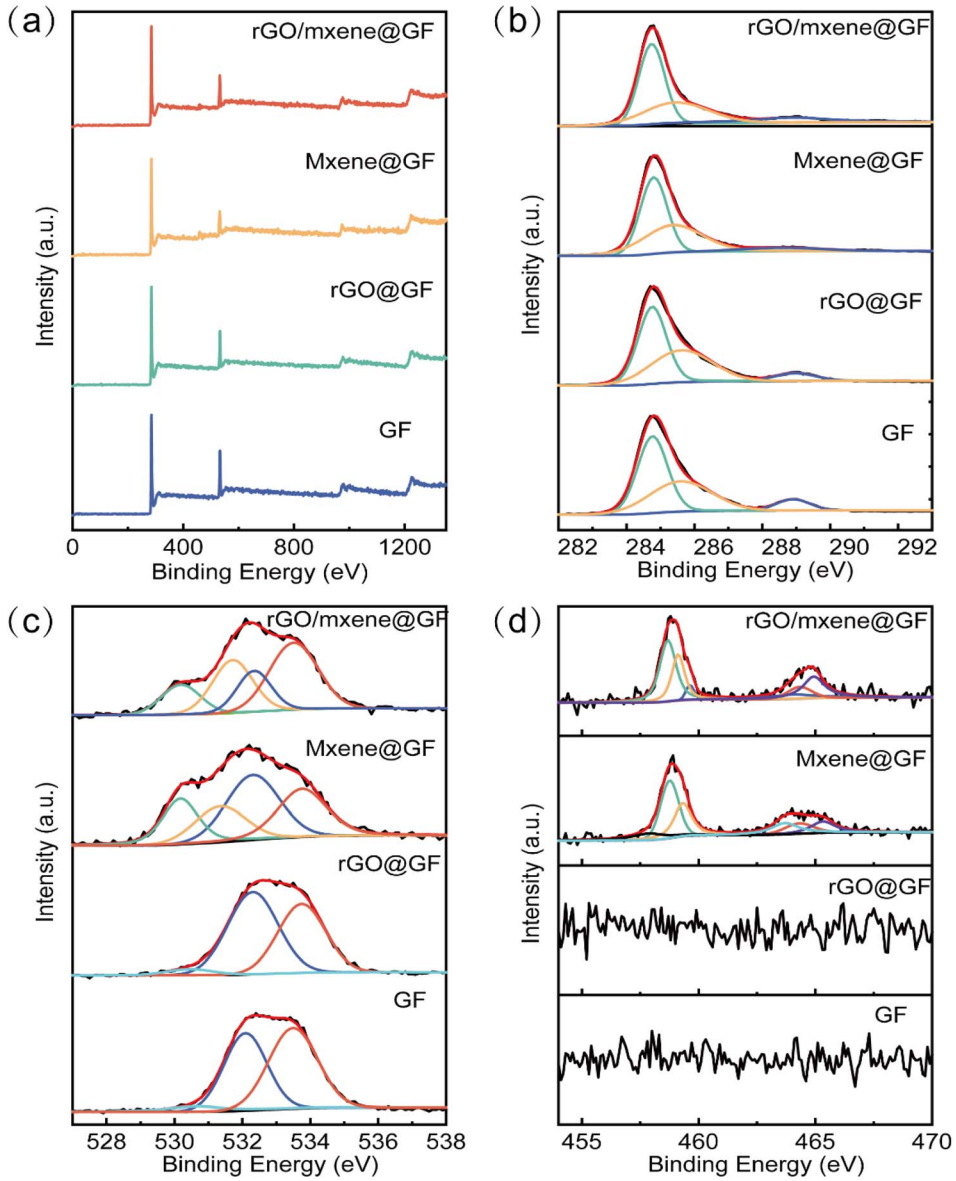

Fig. 5 (a) XPS full spectra, (b) C 1s spectra, (c) O 1s spectra, (d) Ti 2p spectra for different samples.

incorporation of Mxene can tune the microstructure and functional groups on the surface of GF, consequently contributing to the possible improvement of electrochemical reaction kinetics of electrodes.

3.2 Electrochemical performance

The electrochemical performance of the as-prepared electrodes was evaluated through CV tests, which were performed in 0.1 M VO^{2+} + 3 M H_2SO_4 and 0.1 M V^{3+} + 3.0 M H_2SO_4, respectively. As shown in Fig. 6a, it is evident that GF, rGO@GF, Mxene@GF and rGO/Mxene@GF exhibited the oxidation and reduction peak current densities of −40.2/45.7 mA cm^{-2}, −54.7/60.2 mA cm^{-2}, −53.8/59.9 mA cm^{-2} and −68.2/74.3 mA cm^{-2} for VO^{2+}/VO_2^+ redox reactions, separately. Similarly, GF, rGO@GF, Mxene@GF and rGO/Mxene@GF delivered the oxidation and reduction peak current densities of −29.1/19.8 mA cm^{-2}, −36.9/22.3 mA cm^{-2}, −38.1/27.2 mA cm^{-2} and −48.4/35.6 mA cm^{-2} for V^{2+}/V^{3+} redox reactions, respectively (Fig. 6b). From the comparison, it is clear that the rGO/Mxene@GF achieved the highest peak current densities, demonstrating a superior electrochemical performance. In addition, the rGO/Mxene@GF electrodes with different Mxene/rGO ratios were also compared (Fig. S4†), the results indicated that the electrode with 1 : 1 Mxene : rGO delivered the highest current response and lowest charge transfer resistance, indicating the best reaction kinetics. To evaluate the electrochemical reaction kinetics of electrodes, CV tests were carried out at different scanning rates (Fig. 6c and S5†). As shown in Fig. 6d, the CV curves of rGO/Mxene@GF showed the best stability with a peak current density ratio closer to 1 with the increase of scanning rate, consistent with literature reported.[47] To further illustrate the trend in the changes of peak current density for different

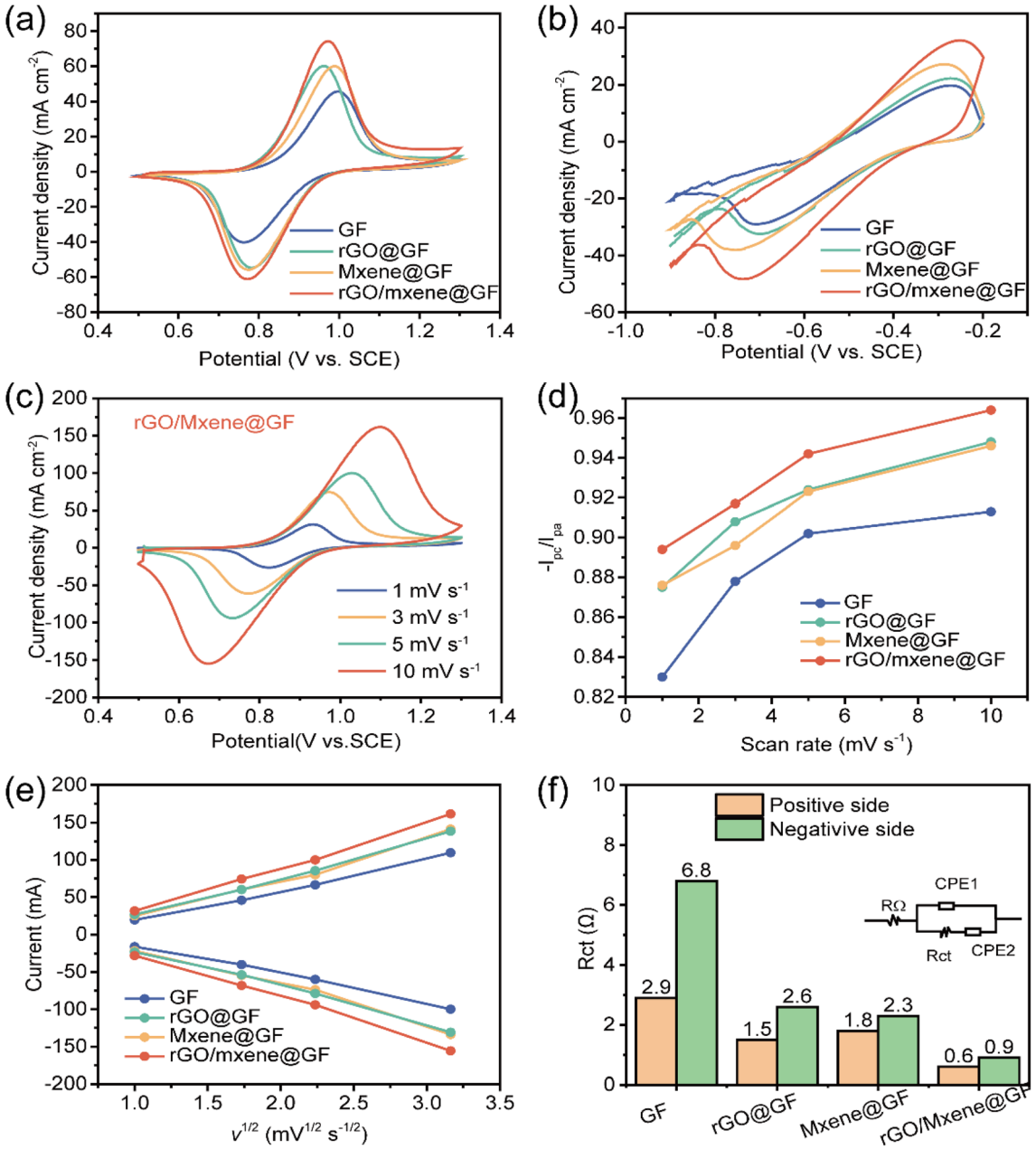

Fig. 6 Electrochemical characterization of GF, rGO@GF, Mxene@GF and rGO/Mxene@GF in 0.1 M VO^{2+} + 3 M H_2SO_4 and 0.1 M V^{3+} + 3.0 M H_2SO_4. (a) CV curves of VO^{2+}/VO_2^+ and (b) CV curves V^{2+}/V^{3+} redox reaction at a scan rate of 3 mV s^{-1}, (c) CV curves of the VO^{2+}/VO_2^+ redox reactions for rGO/Mxene@GF at various scan rates, (d) plots of peak current density ratios *versus* scan rates; (e) plots of peak current density ratios *versus* the square root of scan rates, (f) change transfer resistance.

electrodes, the Randles–Sevcik equation was used to fit the relationship between peak current density and the square root of scan rate, as shown in Fig. 6e. The linear relationship suggests that both forward and reverse reactions are the diffusion-controlled process, the largest slope of rGO/Mxene@GF suggests an enhanced mass transfer, probably due to its improved roughness properties and larger surface area. EIS tests were conducted and Nyquist plots were shown in Fig. S6.† One can see the charge transfer resistance (R_{ct}) remarkably decreased after the incorporation of rGO and Mxene. The R_{ct} was further quantitatively calculated according to the equivalent circuit (Fig. 6f). Among them, the rGO/Mxene@GF exhibited the lowest R_{ct} (0.6–0.9 Ω) during the redox reactions, consistent with the CV results. These findings demonstrate that the prepared rGO/Mxene@GF exhibited the best electrochemical activity, attributing to its larger surface area for the exposure of active sites and the porous structure for improved mass transfer. Although both of rGO and Mxene can improve the electrochemical performance of electrode, the performance increment of electrodes was not distinctive. It is worth noting that the incorporation of both rGO and Mxene remarkably enhanced the electrochemical redox reaction on

electrode, which was probably attributed to the synergistic effect between rGO and $Ti_3C_2T_x$.

3.3 Mass transport of electrodes

The physicochemical and electrochemical characterizations of electrodes have demonstrated the satisfactory electrocatalytic activity of the electrode materials. However, the understanding of mass transfer in electrode is another crucial factor affecting the practical application of electrode. It is widely accepted that a favorable mass transfer behavior in the electrode can effectively improve the battery performance.[48] In general, the mass transfer behavior was significantly influenced by the electrode structure, which results in the changes of the velocity profile and the concentration distribution. To evaluate the mass transfer in electrode, the structure of graphite electrode (rGO/Mxene@GF) was reconstructed based on X-ray computed tomography (Fig. 7a). The selected domain with a size of 0.5 × 0.5 × 0.5 mm was processed using interactive thresholding for geometry building and simulation. The velocity of electrolyte through the 3D electrodes was shown in Fig. 7b, it is clear the maldistribution of velocity was observed in electrode, the velocity in the inner of electrode is larger than that near the boundaries, suggesting a stronger electrolyte flow in the electrode center. This is favorable to the improvement of electrode performance, due to the reason that the electrolyte flow can effective facilitate the ion convection transport. To further identify the mass transfer of electrode, the distribution of V^{2+} and V^{3+} concentration was further calculated, as depicted in Fig. 7c and d. It is evident that the concentration distribution is closely related to the structure of electrode. Although with an uneven concentration distribution, it is clear the changes of V^{2+} and V^{3+} concentration were less than 0.03 mol L^{-1}, the maximum concentration changes were remarkably less than the initial concentration of 0.26 and 1.44 mol L^{-1}. This implies that the changes of V^{2+} and V^{3+} concentration and resulting voltage losses can be neglected. These results concluded that the prepared electrode achieved an efficient mass transfer due to the favorable electrolyte flow through the pore structure of electrode.

3.4 Battery performance

To demonstrate the practical application of the prepared electrodes, the electrodes were actually tested in VRFB (Fig. 8a). The charge–discharge performance was evaluated in a custom-made flow battery with an S-shaped flow field design using different electrodes. As shown in the Fig. 8b–d, the charge–discharge performance of the batteries with prepared electrodes was measured at the current densities of 40, 60 and to 80 mA cm^{-2}, respectively. It is clear that the overpotentials apparently increased for the charge/discharge process with the increase of current density, thus limiting the available voltage window for redox reactions. However, it should be noted that the MXene and/or rGO decorated electrode exhibited a higher specific capacity at various current densities than that of GF electrode,

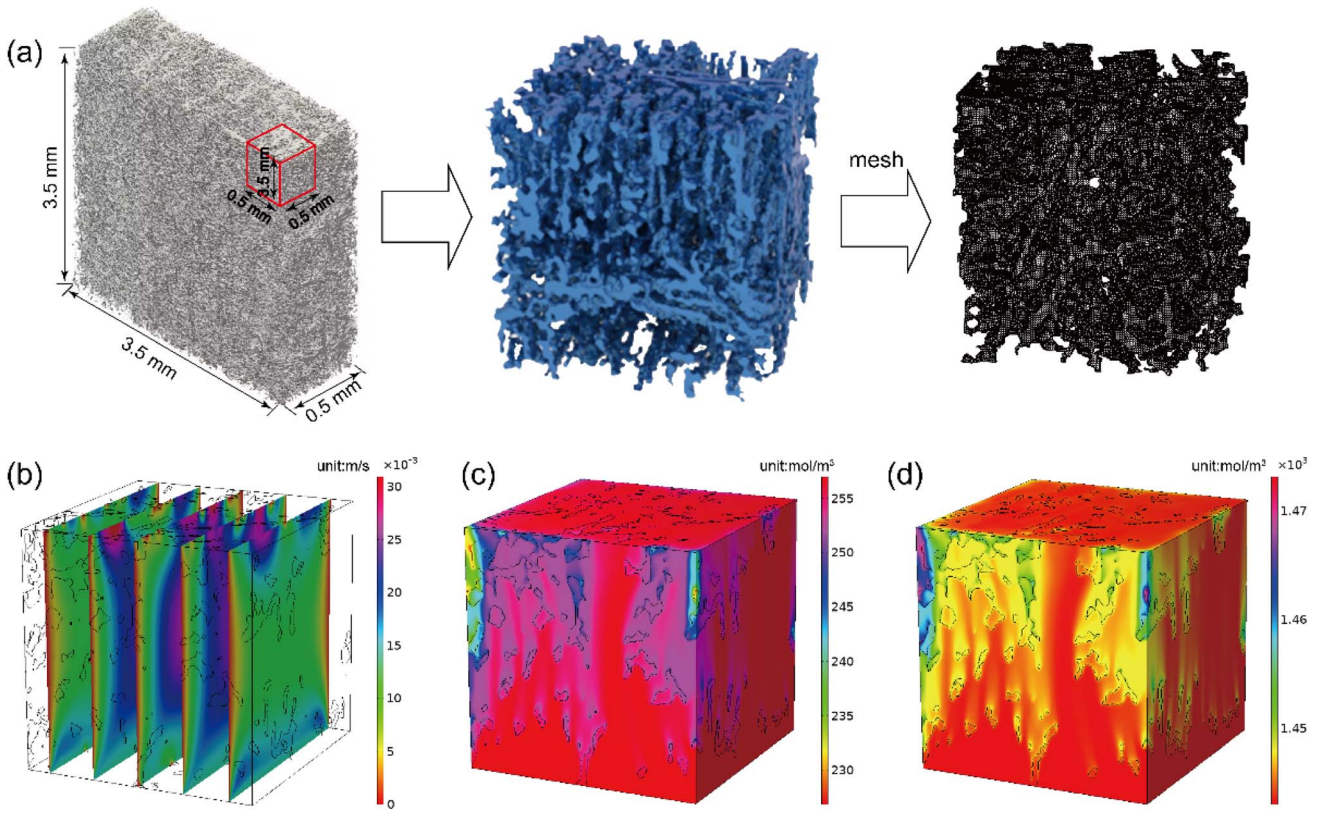

Fig. 7 (a) 3D reconstructed image of the prepared electrode(rGO/Mxene@GF), simulation results of (b) velocity profile, (c) V^{2+} concentration and (d) V^{3+} concentration distributions in electrode at 100 mA cm^{-2}.

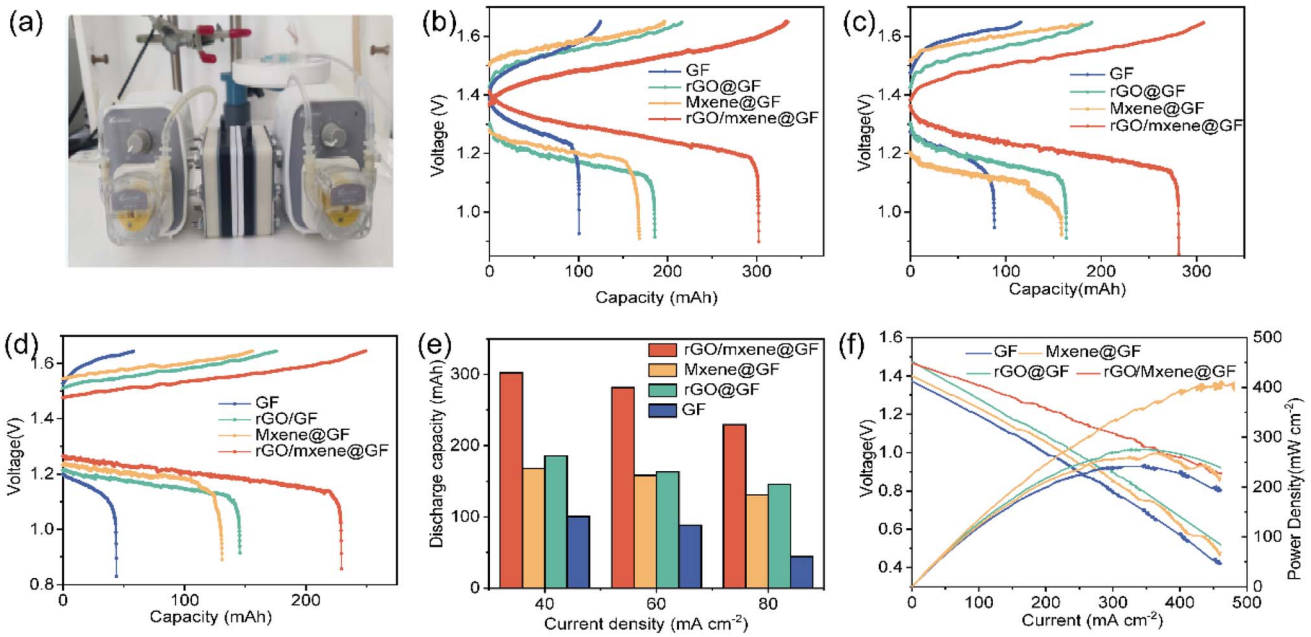

Fig. 8 (a) Picture of battery, charge–discharge curves at (b) 40 mA cm^{-2}, (c) 60 mA cm^{-2}, and (d) 80 mA cm^{-2}, (e) discharge capacities, (f) polarization and power density curves of VRFB.

and the difference becomes much more significant at a higher current density. In detail, the discharge capacity of VRFB with GF, rGO@GF, Mxene@GF and rGO/Mxene@GF was 100.5, 185.6, 168.3 and 302.3 mA h at a current density of 40 mA cm^{-2}, respectively. The discharge capacity of VRFB with rGO/Mxene@GF was 3 times higher than that of GF. Significantly, at a current density of 80 mA cm^{-2}, the discharge capacity of VRFB with GF, rGO@GF, Mxene@GF and rGO/Mxene@GF was 44.1, 145.6, 131.0 and 229.3 mA h, and discharge capacity of VRFB with rGO/Mxene@GF was 5.2 times higher than that of GF (Fig. 8e). These results suggest that the as-prepared electrode can not only improve the capacities but also enable the

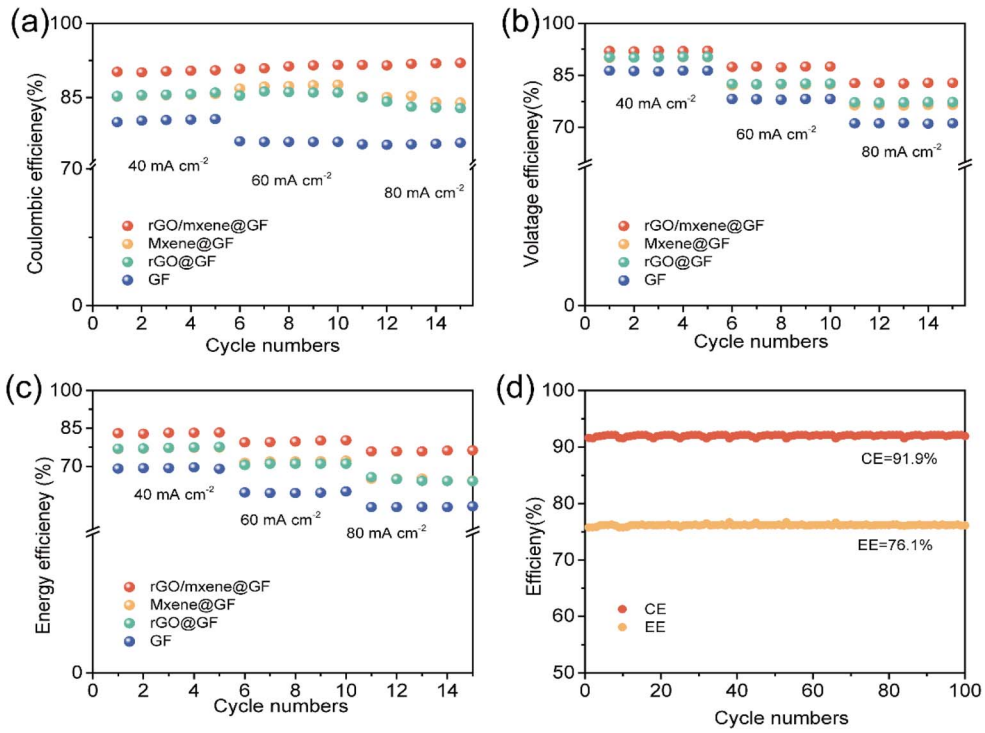

Fig. 9 (a) Coulombic efficiency, (b) voltage efficiency, and (c) energy efficiency of VRFB with different electrodes, (d) cycling performance of VRFB with rGO/Mxene@GF electrode at 80 mA cm^{-2}.

operation at a higher current density in the application of VFRBs. This can be attributed to the reason that the incorporation of rGO/Mxene hybrid effectively lowered the overpotentials for the charge–discharge process, thus widening the available voltage window for VFRB operation and leading to a higher specific capacity. It should be noted that an increased specific capacity can improve the utilization efficiency of electrolyte, thus reducing the cost for VRFB systems and prompting the commercialization of VRFB. In addition, the performance of VEFB was compared based on power density curves, as shown in Fig. 8f. It can be found that the maximum power density of VRFB with GF, rGO@GF, Mxene@GF and rGO/Mxene@GF was 245, 277, 269 and 413 mW cm^{-2}, the VRFB with rGO/Mxene@GF delivered the highest power density output. It can be seen from the polarization curves that the as-prepared electrode in this work can effectively improve current density of flow battery (>400 mA cm^{-2}), higher than those reported in literatures.[49,50]

Furthermore, the coulombic efficiency, voltage efficiency, and energy efficiency of VRFB using different electrodes were further calculated (Fig. 9a–c). It can be seen that the VRFB using rGO/Mxene@GF delivered a high coulombic efficiency over different cycling processes at different current densities, demonstrating a satisfactory performance in the practical applications with the fluctuant power sources. On the contrary, the VRFB using GF, rGO@GF and Mxene@GF exhibited a slight decrease in coulombic efficiency at a current density higher than 60 mA cm^{-2}. Different from the coulombic efficiency, the voltage efficiency and energy efficiency of VRFB decreased with the increase of current density, probably attributing to the larger overpotential and irreversible losses during the redox reactions at a higher current density. Among them, the VRFB using rGO/Mxene@GF exhibited a significantly higher voltage efficiency and energy efficiency. For example, at a current density of 60 mA cm^{-2}, the VRFB using rGO/Mxene@GF delivered the highest energy efficiency of 91.4%, remarkably higher than 87.6% for rGO@GF, 86.0% for Mxene@GF and 76.1% for GF. In addition, the long-term cycling stability of VFRB with rGO/Mxene@GF was verified at 80 mA cm^{-2}. As depicted in Fig. 9d, one can see that the VRFB exhibited a very stable coulombic efficiency of 91.9% and energy efficiency of 76.2% over 100 cycles. These results highlight the long-term cycling stability of VRFB with the prepared electrode in extended durability tests.

4. Conclusion

In this work, we synthesized rGO/Mxene hybrid-decorated graphite felt as an effective electrode for VRFB. In this design, the irregular $Ti_3C_2T_x$ Mxene particles can be dispersed within the graphene layers to increase the exposure of active sites, and a facilitated mass transport of ions can be obtained by using the porous skeleton of graphite felt. The results indicated that the favorable mass transfer and the synergistic effect between rGO and Mxene significantly enhanced the performance of electrode. The VRFB with rGO/Mxene@GF electrode demonstrated a good long-term cycling stability up to 100 cycles with a coulombic, voltage, and energy efficiency of 91.6%, 82.7%, and 75.8% at a current density of 80 mA cm^{-2}. These findings suggest that the as-prepared rGO/Mxene@GF electrode holds a good potential in the application of VRFB, and can provide a possible guidance for the electrode design for electrochemical systems.

Conflicts of interest

The authors declare that they have no known competing financial interests or personal relationships that could have appeared to influence the work reported in this paper.

Acknowledgements

This work was supported by the National Natural Science Foundation of China (No. 52276208), the Natural Science Foundation of Sichuan Province (No. 2022NSFSC0218, 2023NSFSC0835).

References

1 C. Zhang, Z. Niu, S. Peng, Y. Ding, L. Zhang, X. Guo, Y. Zhao and G. Yu, Phenothiazine-Based Organic Catholyte for High-Capacity and Long-Life Aqueous Redox Flow Batteries, *Adv. Mater.*, 2019, **31**(24), 1901052, DOI: 10.1002/adma.201901052.

2 W. Peng, F. Wagner, M. V. Ramana, H. Zhai, M. J. Small, C. Dalin, X. Zhang and D. L. Mauzerall, Managing China's coal power plants to address multiple environmental objectives, *Nat Sustainability*, 2018, **1**(11), 693–701, DOI: 10.1038/s41893-018-0174-1.

3 D. M. Davies, M. G. Verde, O. Mnyshenko, Y. R. Chen, R. Rajeev, Y. S. Meng and G. Elliott, Combined economic and technological evaluation of battery energy storage for grid applications, *Nat. Energy*, 2019, **4**(1), 42–50, DOI: 10.1038/s41560-018-0290-1.

4 D. Zhang, Z. Xu, X. Zhang, L. Zhao, Y. Zhao, S. Wang, W. Liu, X. Che, J. Yang, J. Liu, *et al.*, Oriented Proton-Conductive Nanochannels Boosting a Highly Conductive Proton-Exchange Membrane for a Vanadium Redox Flow Battery, *ACS Appl. Mater. Interfaces*, 2021, **13**(3), 4051–4061, DOI: 10.1021/acsami.0c20847.

5 J. Xu, S. Dong, P. Li, W. Li, F. Tian, J. Wang, Q. Cheng, Z. Yue and H. Yang, Novel ether-free sulfonated poly(biphenyl) tethered with tertiary amine groups as highly stable amphoteric ionic exchange membranes for vanadium redox flow battery, *Chem. Eng. J.*, 2021, **424**, 130314, DOI: 10.1016/j.cej.2021.130314.

6 B. Li, M. Gu, Z. Nie, Y. Shao, Q. Luo, X. Wei, X. Li, J. Xiao, C. Wang, V. Sprenlde, *et al.*, Bismuth Nanoparticle Decorating Graphite Felt as a High-Performance Electrode for an All-Vanadium Redox Flow Battery, *Nano Lett.*, 2013, **13**(3), 1330–1335, DOI: 10.1021/nl400223v.

7 K. Zhang, C. Yan and A. Tang, Oxygen-induced electrode activation and modulation essence towards enhanced anode redox chemistry for vanadium flow batteries, *Energy*

Storage Mater., 2021, **34**, 301–310, DOI: 10.1016/j.ensm.2020.10.005.

8 X. Zang, L. Yan, Y. Yang, H. Pan, Z. Nie, K. W. Jung, Z. D. Deng and W. Wang, Monitoring the State-of-Charge of a Vanadium Redox Flow Battery with the Acoustic Attenuation Coefficient: An In Operando Noninvasive Method, *Small Methods*, 2019, **3**(12), 1900494, DOI: 10.1002/smtd.201900494.

9 M. Yue, Q. Zheng, F. Xing, H. Zhang, X. Li and X. Ma, Flow field design and optimization of high power density vanadium flow batteries: a novel trapezoid flow battery, *AIChE J.*, 2018, **64**(2), 782–795, DOI: 10.1002/aic.15959.

10 D. S. Aaron, Q. Liu, Z. Tang, G. M. Grim, A. B. Papandrew, A. Turhan, T. A. Zawodzinski and M. M. Mench, Dramatic performance gains in vanadium redox flow batteries through modified cell architecture, *J. Power Sources*, 2012, **206**, 450–453, DOI: 10.1016/j.jpowsour.2011.12.026.

11 C. Zhang, L. Zhang, Y. Ding, S. Peng, X. Guo, Y. Zhao, G. He and G. Yu, Progress and prospects of next-generation redox flow batteries, *Energy Storage Mater.*, 2018, **15**, 324–350.

12 K. Percin, A. Rommerskirchen, R. Sengpiel, Y. Gendel and M. Wessling, 3D-printed conductive static mixers enable all-vanadium redox flow battery using slurry electrodes, *J. Power Sources*, 2018, **379**, 228–233, DOI: 10.1016/j.jpowsour.2018.01.061.

13 R. De Wolf, M. De Rop and J. Hereijgers, Effects of Structured 3D Electrodes on the Performance of Redox Flow Batteries, *Chemelectrochem*, 2022, **9**(22), e202200640, DOI: 10.1002/celc.202201028.

14 E. Craddock, R. M. Cuellar-Franca and M. Perez-Page, The incorporation of 2D materials into membranes to improve the environmental sustainability of vanadium redox flow batteries (VRFBs): a critical review, *Curr. Opin. Chem. Eng.*, 2023, **40**, 100906, DOI: 10.1016/j.coche.2023.100906.

15 X. M. Cui, H. B. Ding, X. E. Chen, Z. Y. Zeng, J. Wang and Z. C. Huang, Investigations on the thermal and acid treatment of graphite felt for vanadium redox flow battery application, *Adv. Mater. Res.*, 2014, **953**, 1157–1162, DOI: 10.4028/AMR.953-954.1157.

16 Y. Liu, J. Xu, S. Lu and Y. Xiang, Titanium Nitride Nanorods Array-Decorated Graphite Felt as Highly Efficient Negative Electrode for Iron-Chromium Redox Flow Battery, *Small*, 2023, **19**(32), 2300943, DOI: 10.1002/smll.202300943.

17 P. C. Ghimire, R. Schweiss, G. G. Scherer, T. M. Lim, N. Wai, A. Bhattarai and Q. Yan, Optimization of thermal oxidation of electrodes for the performance enhancement in all-vanadium redox flow batteries, *Carbon*, 2019, **155**, 176–185, DOI: 10.1016/j.carbon.2019.08.068.

18 A. Di Blasi, O. Di Blasi, N. Briguglio, A. S. Arico, D. Sebastian, M. J. Lazaro, G. Monforte and V. Antonucci, Investigation of several graphite-based electrodes for vanadium redox flow cell, *J. Power Sources*, 2013, **227**, 15–23, DOI: 10.1016/j.jpowsour.2012.10.098.

19 X. Wu, H. Xu, P. Xu, Y. Shen, L. Lu, J. Shi, J. Fu and H. Zhao, Microwave-treated graphite felt as the positive electrode for all-vanadium redox flow battery, *J. Power Sources*, 2014, **263**, 104–109, DOI: 10.1016/j.jpowsour.2014.04.035.

20 C. Yu-Chung, C. Jian-Yu, D. M. Kabtamu, L. Guan-Yi, H. Ning-Yih, C. Yi-Sin, W. Hwa-Jou and W. Chen-Hao, High efficiency of CO_2-activated graphite felt as electrode for vanadium redox flow battery application, *J. Power Sources*, 2017, **364**, 1–8, DOI: 10.1016/j.jpowsour.2017.07.103.

21 T. Liu, X. Li, C. Xu and H. Zhang, Activated Carbon Fiber Paper Based Electrodes with High Electrocatalytic Activity for Vanadium Flow Batteries with Improved Power Density, *ACS Appl. Mater. Interfaces*, 2017, **9**(5), 4626–4633, DOI: 10.1021/acsami.6b14478.

22 D. M. Kabtamu, J.-Y. Chen, Y.-C. Chang and C.-H. Wang, Water-activated graphite felt as a high-performance electrode for vanadium redox flow batteries, *J. Power Sources*, 2017, **341**, 270–279, DOI: 10.1016/j.jpowsour.2016.12.004.

23 R. Wang, Y. Li and Y.-L. He, Achieving gradient-pore-oriented graphite felt for vanadium redox flow batteries: meeting improved electrochemical activity and enhanced mass transport from nano-to micro-scale, *J. Mater. Chem. A*, 2019, **7**(18), 10962–10970, DOI: 10.1039/c9ta00807a.

24 Y. Lv, J. Zhang, Z. Lv, C. Wu, Y. Liu, H. Wang, S. Lu and Y. Xiang, Enhanced electrochemical activity of carbon felt for V^{2+}/V^{3+} redox reaction via combining KOH-etched pretreatment with uniform deposition of Bi nanoparticles, *Electrochim. Acta*, 2017, **253**, 78–84, DOI: 10.1016/j.electacta.2017.09.005.

25 H. Agarwal, E. Roy, N. Singh, P. A. Klusener, R. M. Stephens and Q. T. Zhou, Electrode Treatments for Redox Flow Batteries: Translating Our Understanding from Vanadium to Aqueous-Organic, *Advanced Science*, 2023, 2307209.

26 Z. He, Y. Lv, T. Zhang, Y. Zhu, L. Dai, S. Yao, W. Zhu and L. Wang, Electrode materials for vanadium redox flow batteries: intrinsic treatment and introducing catalyst, *Chem. Eng. J.*, 2022, **427**, 131680.

27 Y. Lv, C. Han, Y. Zhu, T. Zhang, S. Yao, Z. He, L. Dai and L. Wang, Recent advances in metals and metal oxides as catalysts for vanadium redox flow battery: properties, structures, and perspectives, *J. Mater. Sci. Technol.*, 2021, **75**, 96–109.

28 Z. Gonzalez, C. Flox, C. Blanco, M. Granda, J. R. Morante, R. Menendez and R. Santamaria, Outstanding electrochemical performance of a graphene-modified graphite felt for vanadium redox flow battery application, *J. Power Sources*, 2017, **338**, 155–162, DOI: 10.1016/j.jpowsour.2016.10.069.

29 X. Wu, H. Xu, L. Lu, H. Zhao, J. Fu, Y. Shen, P. Xu and Y. Dong, PbO_2-modified graphite felt as the positive electrode for an all-vanadium redox flow battery, *J. Power Sources*, 2014, **250**, 274–278, DOI: 10.1016/j.jpowsour.2013.11.021.

30 A. V. Mizrak, S. Uzun, B. Akuzum, L. Agartan, Y. Gogotsi and E. C. Kumbur, Two-Dimensional MXene Modified Electrodes for Improved Anodic Performance in Vanadium Redox Flow Batteries, *J. Electrochem. Soc.*, 2021, **168**(9), 090518, DOI: 10.1149/1945-7111/ac22cd.

31 L. Wei, C. Xiong, H. R. Jiang, X. Z. Fan and T. S. Zhao, Highly catalytic hollow $Ti_3C_2T_x$ MXene spheres decorated graphite felt electrode for vanadium redox flow batteries, *Energy Storage Mater.*, 2020, **25**, 885–892, DOI: **10.1016/j.ensm.2019.08.028**.

32 Y. Song, Z. Li, K. Guo and T. Shao, Hierarchically ordered mesoporous carbon/graphene composites as supercapacitor electrode materials, *Nanoscale*, 2016, **8**(34), 15671–15680, DOI: **10.1039/c6nr04130b**.

33 O. Mashtalir, M. Naguib, V. N. Mochalin, Y. Dall'Agnese, M. Heon, M. W. Barsoum and Y. Gogotsi, Intercalation and delamination of layered carbides and carbonitrides, *Nat. Commun.*, 2013, **4**(1), 1716, DOI: **10.1038/ncomms2664**.

34 C. Zhao, Q. Wang, H. Zhang, S. Passerini and X. Qian, Two-Dimensional Titanium Carbide/RGO Composite for High-Performance Supercapacitors, *ACS Appl. Mater. Interfaces*, 2016, **8**(24), 15661–15667, DOI: **10.1021/acsami.6b04767**.

35 K. S. Novoselov, V. I. Fal'ko, L. Colombo, P. R. Gellert, M. G. Schwab and K. Kim, A roadmap for graphene, *Nature*, 2012, **490**(7419), 192–200, DOI: **10.1038/nature11458**.

36 H. Li, Y. Hou, F. Wang, M. R. Lohe, X. Zhuang, L. Niu and X. Feng, Flexible All-Solid-State Supercapacitors with High Volumetric Capacitances Boosted by Solution Processable MXene and Electrochemically Exfoliated Graphene, *Adv. Energy Mater.*, 2017, **7**(4), 1601847, DOI: **10.1002/aenm.201601847**.

37 M.-Q. Zhao, X. Xie, C. E. Ren, T. Makaryan, B. Anasori, G. Wang and Y. Gogotsi, Hollow MXene Spheres and 3D Macroporous MXene Frameworks for Na-Ion Storage, *Adv. Mater.*, 2017, **29**(37), 1702410, DOI: **10.1002/adma.201702410**.

38 K. Wang, B. Zheng, M. Mackinder, N. Baule, H. Qiao, H. Jin, T. Schuelke and Q. H. Fan, Graphene wrapped MXene *via* plasma exfoliation for all-solid-state flexible supercapacitors, *Energy Storage Mater.*, 2019, **20**, 299–306, DOI: **10.1016/j.ensm.2019.04.029**.

39 J. Zheng, J. Zhang, P. Xu, J. Li and W. Yang, Interface design for enhancing carbon dioxide electrolysis in a fluidized electrode of photoelectrochemical cell, *Chem. Eng. J.*, 2022, **450**, 138158.

40 S. Chen, H. Ren, Y. Qiu, C. Luo, Q. Zhao and W. Yang, Engineering bifunctional electrocatalysts for rechargeable Zn-Air battery by confining Co–Zn–Mn in flower-structured carbon, *J. Power Sources*, 2023, **573**, 233116.

41 S. Kumar, M. A. Rehman, S. Lee, M. Kim, H. Hong, J.-Y. Park and Y. Seo, Supercapacitors based on $Ti_3C_2T_x$ MXene extracted from supernatant and current collectors passivated by CVD-graphene, *Sci. Rep.*, 2021, **11**(1), 649, DOI: **10.1038/s41598-020-80799-9**.

42 N. Talreja, M. Ashfaq, D. Chauhan and R. V. Mangalaraja, Cu-MXene: a potential biocide for the next-generation biomedical application, *Mater. Chem. Phys.*, 2023, **294**, 127029, DOI: **10.1016/j.matchemphys.2022.127029**.

43 M. Boota, I. Ahmad and J. Ahmad, Production of graphene-derivatives using organic molecules for supercapacitors and beyond, *Colloids Surf., A*, 2023, **658**, 130693, DOI: **10.1016/j.colsurfa.2022.130693**.

44 H. Chen, G. Ke, X. Wu, W. Li, Y. Li, H. Mi, L. Sun, Q. Zhang, C. He and X. Ren, Amorphous MoS_3 decoration on 2D functionalized MXene as a bifunctional electrode for stable and robust lithium storage, *Chem. Eng. J.*, 2021, **406**, 126775.

45 Z. Wang, Z. Xu, H. Huang, X. Chu, Y. Xie, D. Xiong, C. Yan, H. Zhao, H. Zhang and W. Yang, Unraveling and regulating self-discharge behavior of $Ti_3C_2T_x$ MXene-based supercapacitors, *ACS Nano*, 2020, **14**(4), 4916–4924.

46 C. Zhang, Z. Wu, C. Xu, B. Yang, L. Wang, W. You and R. Che, Hierarchical $Ti_3C_2T_x$ MXene/carbon nanotubes hollow microsphere with confined magnetic nanospheres for broadband microwave absorption, *Small*, 2022, **18**(3), 2104380.

47 X. Zhang, D. Zhang, Z. Xu, K. Zhang, Y. Zhang, M. Jing, L. Liu, Z. Zhang, N. Pu and J. Liu, A pioneering melamine foam-based electrode via facile synthesis as prospective direction for vanadium redox flow batteries, *Chem. Eng. J.*, 2022, **439**, 135718.

48 F. Chu, M. Su, G. Xiao, Z. Tan and G. Yang, Analysis of electrode configuration effects on mass transfer and organic redox flow battery performance, *Ind. Eng. Chem. Res.*, 2022, **61**(7), 2915–2925.

49 R. Cheng, J. Xu, J. Zhang, P. Leung, Q. Ma, H. Su, W. Yang and Q. Xu, Facile segmented graphite felt electrode for iron-vanadium redox flow batteries with deep eutectic solvent (DES) electrolyte, *J. Power Sources*, 2021, **483**, 229200.

50 Z. Tang, J. Zou, D. Zhang, X. Chen, Y. Yu, K. Huang and Z. Xu, Ti_xO_y loaded carbon felt as high performance negative for vanadium redox flow battery, *J. Power Sources*, 2023, **566**, 232925.